Imaging perfusion using hyperpolarized ^{129}Xe MRI and [^{15}O]-water PET: Current status and future clinical applications

Ramanpreet K Sembhi[1]; Matt S Fox[1,2]; Alexei V Ouriadov[1,2,3]*

[1]Department of Physics and Astronomy, the University of Western Ontario, London, Ontario, Canada.

[2]Lawson Health Research Institute, London, Ontario, Canada.

[3]School of Biomedical Engineering, Faculty of Engineering, the University of Western Ontario, London, Ontario, Canada.

*Corresponding Author: Alexei V Ouriadov

The University of Western Ontario, 1151 Richmond Street London, Ontario, Canada, N6A 3K7. Canada.

Tel: 1-519-670-0641; Email: aouriado@uwo.ca

Abstract

Inhaled hyperpolarized ^{129}Xe MRI is a non-invasive imaging technique for assessing lung structure and function. Not only within lung, ^{129}Xe MRI has proven to be effective for functional and structural imaging of the brain and other organs. These measurements are possible due to a distinct and wide range of chemical shift frequencies (~200 ppm) of ^{129}Xe when residing within lung tissue, brain tissue and red blood cells compared to the gas phase. Due to a range of physical characteristics of the ^{129}Xe isotope that makes it advantageous for brain scans, it might be used as a new probe for brain blood flow, grey and white matter mapping, and functional assessments. When employed for functional imaging, such as perfusion imaging, hyperpolarized ^{129}Xe dissolves in the pulmonary circulation and goes to the brain with the blood flow. [^{15}O]-water PET is the gold standard imaging technique for assessing cerebral perfusion. ^{15}O isotopes have a short half-life, diffuse easily and are metabolically inert, just like ^{129}Xe and because of these characteristics, it's ideal for non-invasive imaging-based perfusion evaluations. As a result of the human ^{129}Xe lung and brain MRI studies that have already been documented in the literature and taking in account the FDA (Food and Drug Administration) approval of ^{129}Xe lung MRI, the primary goal of this review is to focus on the potential applications of ^{129}Xe brain imaging in comparison to the gold standard perfusing imaging technique [^{15}O]-water PET to clinical approval of ^{129}Xe brain MRI and it wide use. The *in-vivo* uses of ^{129}Xe MRI and ^{15}O-gas/water PET to investigate lung ventilation/perfusion, gas exchange, blood oxygenation, cerebral perfusion in humans as well as animals are reviewed in this article. It also focusses on hybrid PET/MRI techniques developed recently allowing non-invasive *in-vivo* brain perfusion monitoring. This article briefly covers the challenges, limitations and opportunities of both imaging modalities. In recent work by our group, the possibility of a single-shot, multi-modal-imaging technique utilising simultaneous PET/MRI was illustrated, for the first time on a global scale. The similarity between images obtained from both imaging modalities and tracers indicates that the xenon imaging approach could be used to monitor brain perfusion in the future.

Hyperpolarized [129]xe MRI

Physical Properties of [129]Xe

Xenon is a noble gas that has nine naturally occurring isotopes, but only two of these, [129]Xe and [131]Xe are suitable for magnetic resonance giving their non-zero spin. [129]Xe is an extremely stable, monoatomic, spin ½, and naturally abundant isotope constituting 26% of natural xenon [1] possessing a higher gyromagnetic ratio compared to [131]Xe [2] with value of 11.78 MHz/T [3]. However, it is almost 3 times smaller than the gyromagnetic ratio of [1]H. The self-diffusion coefficient of [129]Xe is 0.062 cm^2/s [4] . The estimated cost (in CAD) of enriched (86%) [129]Xe is $2,000.00/L while the cost of naturally abundant [129]Xe is $500.00/L. [129]Xe does not have a quadrupole moment but, has a higher longitudinal relaxation duration after it is polarised [5]. Xenon can be used to examine its chemical environment [6] efficiently because it is inert and monoatomic and has a vast spherical electron cloud, which when distorted, impacts the Nuclear Magnetic Resonance (NMR) chemical shift. The thermally polarized [129]Xe cannot be used in MR imaging due to the low gas density and low gyromagnetic ratio which results in a low image quality due to negligible xenon signal. This difficulty can be solved by polarizing [129]Xe before the scans using spin-exchange optical pumping, which enhances the spin polarization up to five orders of magnitude [3], further resulting in a rise in MRI signal strength.

Xenon is a fast-acting anesthesia [7,8]. When xenon concentrations in the alveoli are more than 70%, anaesthetic effects [7,8] can occur. Xenon has been utilized as an anesthesia for the last few years, and patients have experienced no serious side effects other than minor dizziness [9]. Inhaled xenon can be employed safely for MR imaging. A study by Shukla et al. [10] on 33 subjects, including both healthy and patients with COPD revealed no side effects on administering 1 litre dose of [129]Xe and [4]He gas mixed in equal proportions. In another study, participants inhaled a gas dose of 1 litre of [129]Xe from a bag using a filtration breather for 2 seconds, and no serious anaesthetic effects were found in the individuals, according to Rao et al. [11].

Table 1: Enlists some of the important physical parameters of [129]Xe that makes it effective for imaging.

Physical Properties of [129]Xe	
Parameters	**Values for [129]Xe**
Nuclear Spin, I	1/2
Gyromagnetic ratio, γ(MHz/T)	11.78
Natural abundance (%)	26
Apparent Transverse Relaxation Time, T_2* (ms)	2.8[a]/2.9[b]
Longitudinal Relaxation Time, T_1 (s)	25[c]
Self-diffusion coef., D_0 $(cm^2$/s) [12]	0.062
Diffusion coef. in air, D $(cm^2$/s) [12]	0.14
Chemical shift range, Δδ (ppm)	220
Ostwald solubility (L)	0.17[d]

T_2* values shown correspond to xenon gas (a) within major airway and (b) dissolved within lung tissue (barrier) and red blood cells. T_1 value (c) is measured in rodent lungs after several wash-out (anoxic) breaths of the hyperpolarized gas [12]. (d) at body temperature and atmospheric pressure [3].

[129]Xe Polarization

Even though it is feasible to scan thermally polarized [129]Xe by placing it in a MR scanner, but the low density of gas will produce a signal too low to be useful for imaging. The nuclear polarization can be raised by a factor of ten thousand times [3] than that of thermal equilibrium polarization using the hyperpolarization process. As a consequence, the MR signal from the hyperpolarized noble gas is enhanced, making it easy to identify with an MR scanner tuned to the proper resonance frequency [13]. [129]Xe can be polarized up to nearly 50% [5,9] with the help of Spin Exchange Optical Pumping (SEOP) [14,15]. In this process, alkali-metal such as rubidium gets vaporized and transfer polarization from circularly polarized laser light to noble-gas atoms [16] through collision. At typical operating parameters, the rubidium vapor pressure is only about 1ppm that of the gas in the cell, so it's a very dilute vapor of rubidium. The majority of the alkali-metal remains as a liquid in the optical cell. The rubidium electrons become oriented again by absorbing more laser light after the spin-exchange collision and continue to create polarization within [129]Xe gas nuclei. When a combination of 1% [129]Xe, 89% [4]He, and 10% N_2 is directed to flow through the optical cell and interact with the optically pumped [87]Rb atoms, spin exchange occurs [17], thereby increasing the polarization of [129]Xe. Two types of cells are used in the commercial polarizers that are categorized as static cell and flowing cells [18-21]. In terms of flowing cell polarizers, recently, Hersman et al. [5] Used a continuous flow system operating at low pressure and high velocity to demonstrate a new technology for generating highly polarized xenon in huge quantities. There were various sections of the main cell that were capable of simultaneously vaporising, condensing rubidium along with polarizing xenon [5]. The most significant benefit of this technology was that following a freeze-thaw cycle, the polarization was not lost and was dissipated only when used for higher flow rates. This approach proved successful in creating ~50% polarization at a rate of 0.3litre/hr and is currently being employed in human lung imaging studies [22]. A compact version of this unique concept is being under development which will be beneficial for clinical environment.

Another example of the modified continuous flow cell polarizer is recently constructed by Norquay et al. with a cell volume of 3500cm^3 that can produce 35% polarization at a rate of production of 1.2 litre/hr [23]. This polarizer was utilized in a clinical environment to perform [129]Xe lung and brain scans [22]. Furthermore, this group has achieved the calculated theoretical limit [24] of 86% polarization of [129]Xe by employing a continuous-flow SEOP apparatus, leading to high quality pulmonary imaging.

One of a new [129]Xe polarizers [25] is a static, semi-automated flowing xenon cell polarizer. Xenon polarized by this polarizer is certified and approved for clinical studies [26]. The polarization lies in a range of 35-45% [18] with production rate of 1-3 litre/hr. Alternatively, a fully automated static cell apparatus available currently [19] enables up to 50% xenon polarization [19] and does not require constant liquid nitrogen use (avoiding the freeze-thaw cycle and lowering polarizer usage costs). It has the ability to produce polarized xenon at a rate of 1 litr/hr. Another benefit of using static-cell polarizer over a flowing polarizer design is its ability to keep the expensive [129]Xe (86% enrichment

factor) isotope inside the cell if [129]Xe MRI measurements are not immediately possible for some reason, thus, saving thousands of dollars each time. Presently, there are three firms [18,27] that sell high polarization level xenon polarizers in large quantity which have almost identical gas volume generation rates and xenon polarization levels.

Gas Phase Pulmonary [129]Xe MRI

Inhaled hyperpolarized [129]Xe MRI is a non-invasive and radiation-free imaging technology. Initially, it was the idea of Mitchell Albert who wanted to see how anaesthesia affects the brain [9], so he tried to use [129]Xe to scan it directly. However, desirable polarization could not be achieved, hence Albert et al. used [129]Xe MRI to image the lungs [28]. MR imaging of gaseous-phase hyperpolarized [129]Xe during a sustained breath-hold can yield detailed 3D images of the lungs' ventilated airspaces [6]. The most often used ventilation imaging technique allows to calculate the Ventilation Defect Percentage (VDP) by overlapping the [129]Xe MRI and ^{1}H MRI lung images [29-33]. VDP calculated by hyperpolarized [129]Xe MR imaging can detect regional ventilation and has a strong relationship with pulmonary function testing [31]. When comparing patients with Chronic Obstructive Pulmonary Disease (COPD), asthma, Cystic Fibrosis (CF), and lung cancer to healthy volunteers [6,32, 34-37], [129]Xe ventilation imaging shows higher ventilation heterogeneity and VDP. Even in people with airway function impairment not detected by spirometry, quantitative [129]Xe MRI provides a reliable and objective means of displaying and quantifying the pulmonary ventilation distribution[34]. A study by Kirby et al. [35] was conducted on healthy humans and COPD patients to compare the hyperpolarized [129]Xe MR imaging with that of [3]He imaging and found that the VDP obtained with the former technique was considerably higher than that obtained with the latter in patients with COPD in contrast to healthy volunteers, indicating inadequate or delayed lung filling that may be due to anatomical abnormalities in COPD. In another study by Ebner et al. [36] Ventilation Defect Score (VDS) was measured for a group consisting of healthy people, patients with asthma and patients suffering from COPD and the study revealed that the VDS, as evaluated by hyperpolarized [129]Xe-MRI, corresponds to the severity of airway obstruction and differs considerably between healthy control participants and patients with mild and moderate airway obstruction [36]. The ability of hyperpolarized [129]Xe-MRI to portray illness severity at an early stage is demonstrated by these findings. A study conducted by Thomen et al. on patients of cystic fibrosis and healthy individuals [32] used gold standard forced expiratory volume (FEV$_1$) to quantify lung diseases and compared the results with VDP measured using [129]Xe-MRI. These findings showed that hyperpolarized [129]Xe was far more sensitive than FEV$_1$ in diagnosing CF lung illness and distinguishing CF patients from healthy controls. In a comparison study conducted by Stewart et al. [37], it was demonstrated that patients with Non-Small-Cell Lung Cancer (NSCLC) had significant ventilation anomalies, with most showing a heterogeneous distribution of ventilated airspaces and complete lack of ventilation in the lung region linked with malignancies. Also, it was found that most of the COPD patients had severe ventilation problems, with entire lobes of the lungs frequently found to be completely devoid of air. All of these studies showed that regional functional ventilation deficits can be detected early on in individuals with lung

diseases using hyperpolarized [129]Xe MRI, which cannot be detected by other imaging modalities and thus, allowing for the commencement of treatment before the disease worsens.

Dissolved phase pulmonary [129]Xe MRI

[129]Xe MRI approach offers a mechanism to observe and measure the parts of the lung that participate in Ventilation/Perfusion (V/P), as well as those that do not. Xenon dissolves in the respiratory bloodstream in the same way that oxygen does [38]. Due to xenon's inherent solubility in lung tissue (Ostwald solubility coefficient of 0.17L [3]) and large chemical shift, simultaneous V/P lung measurements of functional gas exchange within the lungs are possible. Figure 1 depicts three different resonances for [129]Xe in red blood cells, [129]Xe in tissue (barrier), and free [129]Xe in the airspaces.
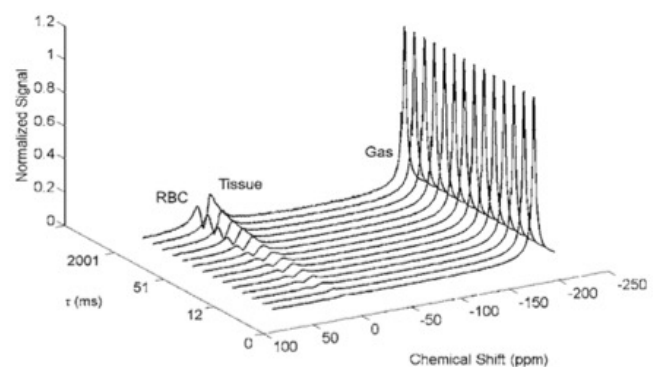

Figure 1: Representative temporally resolved whole-rat-lung [129]Xe spectrum shows three different resonances corresponding to [129]Xe gas phase, [129]Xe dissolved in tissue and [129]Xe bounded to red blood cells. The chemical shift between gas phase and dissolved phase is around 200 ppm. The chemical shift between xenon in lung tissue and blood is around 6ppm. Figure was adapted from [39].

The peaks corresponding to air and red blood cells had shifted by about 200ppm [40]. Because xenon's solubility in aqueous conditions is generally low, this led to most of the [129]Xe escaping and entering the airspaces. That's why, airborne [129]Xe signal was much bigger than the dissolved [129]Xe signal [41]. Miller et al. [1] discovered a wide range of discrete chemical shifts of [129]Xe (which are a function of temperature and density) in different substances and tissues with a linewidth of 1-2 Hz, making it a useful probe for studying biological systems.

Hyperpolarized [129]Xe MRI was proven to be useful for the observation and treatment planning of several pulmonary diseases including COPD, asthma, and lung cancer [31,32,35,36,42,43]. Various studies in both humans and animals have demonstrated the benefit of utilising dissolved phase hyperpolarized [129]Xe MRI to identify the distribution of xenon [44,45] in the lungs as well as to diagnose lung diseases [43,46]. A study by Swanson et al. [47] used healthy rats and demonstrated the first direct imaging of dissolved phase [129]Xe with the help of chemical-shift imaging technique ensuring that the [129]Xe signal was broadly confined to the thorax only and not to the lung's gas-exchange areas.

Driehuys et al. [44] demonstrated less invasive method for studying gas exchange and pulmonary perfusion by collecting images from healthy rats after vascular injection of [129]Xe-saline mixture. This method depended on the specific detection of

only the gaseous [129]Xe that arises in the lungs' airspaces [41], and hence pulmonary function can be assessed indirectly using it. In addition to it, a study by Fox et al. [39] discovered inflammation in the lungs of rats two weeks after irradiation. To establish the early effects of Radiation-Induced Lung Injury (RILI), which is a common side-effect that occurs in patients undergoing radiotherapy, the difference in xenon transfer time constants in tissue and red blood cells was investigated. Also, an increase in xenon transfer time for tissues was observed due to significant thickening of the blood brain barrier.

Despite the animal studies, recent literature has described lung imaging using dissolved phase [129]Xe MRI in humans as well. In a study by Cleveland *et al.* [48], 3D dissolved [129]Xe lung pictures in a single breath-hold were effectively produced while evaluating the regional absorption of alveolar gases in healthy humans. Kaushik *et al.* [24] acquired 3D images of [129]Xe distributed in barrier and red blood cells, as well as gas phase images, to show that the gas-transfer defect present in the peripheral and basal lung of a person with Idiopathic Pulmonary Fibrosis (IPF) was two times greater than that of a healthy person. This is because the signal intensity of dissolved [129]Xe reduces as it travels through the damaged tissues. Ruppert et al [42]. Quantified the apparent diffusion coefficient of the gas phase and evaluated functional alveolar wall thickness utilising [129]Xe chemical shift saturation recovery spectroscopy [43]. The experiment included smokers with Chronic Obstructive Pulmonary Disease (COPD), healthy smokers, and healthy non-smokers of the same age. The difference in septal wall thickness determined per year between healthy participants, COPD patients, and healthy smokers was quite substantial, making this technique an important tool for early detection of lung illnesses.

Kidney [129]Xe MRI

It is very difficult to detect chronic kidney diseases at an early stage because if one kidney is compromised, the other kidney is sufficient to balance its functioning. Traditional methods based on glomerular filtration rates are not able to discover anomalies until both kidneys' function has been substantially compromised [49]. Zollner et al. studied the effect on parameters used in MR due to changes in the kidney functioning in rats with the help of dynamic contrast-enhanced MRI [50], which is an invasive technique of measuring tissue perfusion. The results of the study revealed that tubular flow, and hence GFR, may be a valuable metric for detecting abnormalities in renal tissue in case of acute kidney injury. Hence in order to identify early abnormalities in kidneys, various techniques using biomarkers [49] such as ^{1}H MRI (Arterial Spin Labelling (ASL)) [51,52] has been employed. Despite the fact that ASL is harmless to use, it has not been able to provide unchanging perfusion parameters because multiple repetitions and a large field (3T) are required in ASL due to its low SNR [53,54]. Since [129]Xe dissolves rapidly in blood upon intake (T_1 of [129]Xe in blood is 8 seconds [55]), it could be used to image the kidneys, as these are one of the body's best-perfused organs. Mugler et al. [56] performed preliminary 1.5T MRI of kidneys. Recently, Miller et al. [57] likewise employed spectroscopic technique to examine the kinetics of [129]Xe uptake in an individual human kidney. The latest research assessing the absorption of dissolved [129]Xe in human kidneys was investigated on three healthy subjects by Caldera *et al.* [49] group revealing the possibility of using hyperpolarized [129]Xe MR as a unique and safe approach for evaluating renal perfusion.

Brain [129]Xe MRI

Recent years have seen the development of xenon's ability to view the brain beyond the lungs. When xenon is dissolved in the bloodstream, it is circulated to the brain. Swanson et al. [58] demonstrated the initial in-vivo animal brain spectra using [129]Xe and found the dissolved phase peak located at 194.5 ppm but the polarization of xenon was low, and to acquire high temporal and spatial resolution of brain imaging, polarization should be high. Wakai et al. [59] enhanced the polarization with advanced technology and studied the brain spectra of healthy rats while making them breathe continuously. Figure 2 shows that the head spectra was acquired over a wide range of chemical shifts, ranging from 189 to 210 ppm [59], with the gas phase set at 0 ppm.
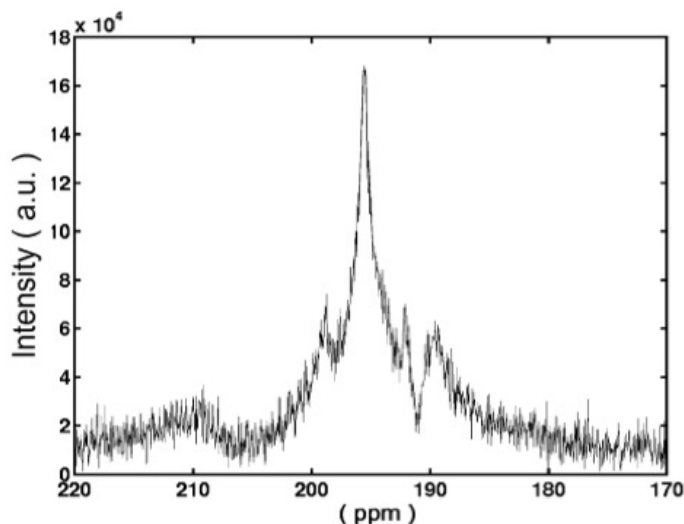

Figure 2: The spectra corresponding to nuclear magnetic resonance of 129Xe in the rat head were obtained by setting the gas phase maximum at 0ppm. The 210-ppm peak was attributed to blood, while the 196-ppm peak was attributed solely to brain tissue. Two additional peaks, at 189 and 199 ppm, were discovered but not ascribed to any tissue. The spectrum was generated using an average of 60 captures with a 1s repetition time. Figure was adapted from [59].

Although the peak at 196 ppm was previously given to tissue and blood [58,60], the peak corresponding to 210 ppm was also seen in the chest spectra of rats during this study, therefore it was re-assigned to blood and the peak at 196 ppm was deemed only from brain tissue. The spectrum also revealed two more peaks. To further establish the existence of five peaks and to demonstrate the source of unidentified peaks in rat head spectra, Kershaw *et al.* conducted an experiment employing ligations of the external carotid artery (ECA) and the Pterygopalatine Artery (PPA) in which the same animal was used pre- and post-ligation. Figure 3 shows that after the ligations, the peaks from non-brain tissues vanished totally, however the peaks from brain tissue were present, and these peaks were ascribed to grey matter (193-197 ppm) and white matter (191-194 ppm) correspondingly [61].
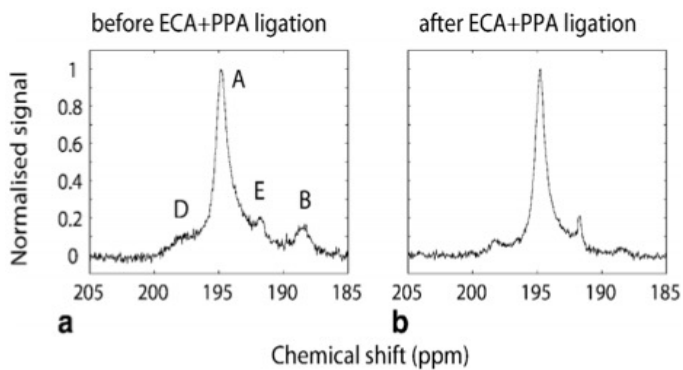
Figure 3: Peaks B and D are noticeably suppressed in the dissolved phase spectrum acquired from the same rat, while A (gray matter) and E (white matter) persist even after employing ligations. Shimming effects and modifying the anaesthetic had no discernible influence on the inconsistencies of other peaks, according to the study. Figure was adapted from [61].

Figure 4: (A) Using a 3T scanner, a pseudo continuous arterial spin-labelling image is acquired for comparison with [129]Xe image. (B) Hyperpolarized [129]Xe *in-vivo* image was obtained for a healthy individual by averaging four images, three of which were acquired during a breath-hold at an interval of 8 seconds, 16 seconds, and 24 seconds with the fourth image taken after the breathing was resumed at 32 seconds. Despite having a higher resolution than the [129]Xe image, the ASL image has an undesired signal outside the brain (indicated by the arrow), which is not present in the [129]Xe dissolved phase image, indicating that latter image was acquired from the signal originating solely from the brain tissue. (C) In an axial pseudo continuous ASL image, hyperintensity is found in the cortex around the blockage. (D) Post-stroke imaging was performed on a male subject. Using hyperpolarized [129]Xe imaging, it is observed that the absorption in the brain tissue fed by the left internal carotid artery was suppressed. In the hypo-intensity region of the picture, there is a signal loss of approximately 60% when compared to the healthy parts. Figures were adapted from [11,64].

The first *in-vivo* human brain spectrum was demonstrated by Mugler et al. using a healthy human volunteer. The dissolved phase of [129]Xe in the brain was detected at 196ppm [62] on the spectrum. Furthermore, Rao *et al.* conducted an experiment on three healthy human individuals to determine the clinical feasibility of imaging the human brain using hyperpolarized [129]Xe MRI. Dissolved [129]Xe MR images were obtained by having them breath hyperpolarized [129]Xe gas [11]. There was no need for any injections in this process, therefore it was performed at minimal risk. Moreover, because inhaled [129]Xe passes the blood-brain barrier and enters extravascular tissue compartments [63], this study was able to image perfusion directly. The images acquired are shown here in Figures 4 (A) and (B) in which [129]Xe MR images were compared to perfusion images obtained using arterial spin labelling and traditional proton imaging techniques to verify the findings.

Although the images were structurally comparable, there was an undesired signal outside the brain in the ASL image, whereas the dissolved [129]Xe MR image solely showed signal from the brain. Additionally, none of the patients in this study underwent anaesthesia, proving that it has more considerable benefits. Later, a study on five healthy individuals was undertaken and xenon perfusion model [65] was built using ^{1}H images that showed blood perfusion and water uptake in grey matter, and the results were compared to [129]Xe brain images displaying xenon perfusion. For a 26-year-old healthy participant, a reasonable spatial correlation factor of 0.53 was found between cerebral perfusion and gas uptake in the brain. This research demonstrated that combining the distinguished features of water and [129]Xe can be useful in better understanding of gas exchange across the blood-brain barrier.

Despite low signal of [129]Xe in brain, in a rat paradigm, Zhou *et al.* presented the first use of *in vivo* ischemic stroke imaging [66] with hyperpolarized [129]Xe brain Chemical Shift Imaging (CSI). [129]Xe image revealed an area with a weak signal that corresponded to the ischemic core. Histology and standard diffusion weighted imaging both provided confirmation of these findings. Mazzanti et al. research was the first to show that rat brain sensory stimulation could be detected and mapped using [129]Xe brain MRI [67]. The authors found that the brain regions in charge of processing pain showed a rise in the signal in 2D [129]Xe CSI images taken before and after stimulation from injection of capsaicin into the forepaw. Not only that, but a study by
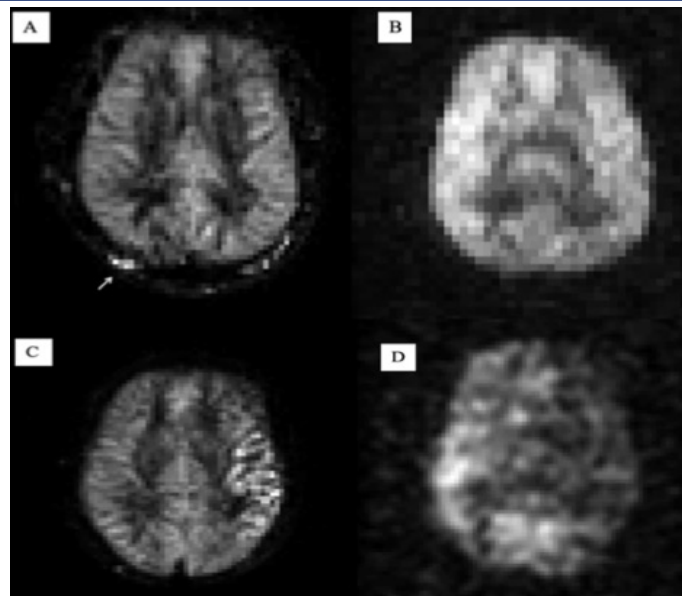
Rao et al. [64] established the clinical effectiveness of brain MRI employing hyperpolarized [129]Xe to a person who suffered from a stroke due to blockage in the left internal carotid artery. Figure 4 (C) and (D) reveals the comparison of ASL and [129]Xe images showing that the amount of perfused xenon in the brain tissue fed by the injured artery was found to be lower as compared to the healthy part. This result could be significant in assessing the chances of next stroke. This research showed a significant difference from previously utilised imaging methods for evaluating gas intake and cerebral tissue perfusion in the region of interest.

[129]Xe MRI is emerging as an excellent method for imaging both healthy and diseased brains since it is safe to inhale and has specific solubility and wide and distinct range of chemical shift in certain tissues. [129]Xe-based imaging has the potential to revolutionise existing imaging technologies as it could provide quick and direct perfusion imaging, even at low field, with an SNR equivalent to ASL perfusion imaging[68] . Furthermore, the blood brain barrier (BBB) surface area and changes in barrier permeability/transferability[69, 70] may be further understood by taking into account xenon's capacity to penetrate the BBB.

Positron Emission Tomography (PET)

Use of different radiotracers

In this technique, anti-matter of electrons, positrons are used. They interact through an annihilation event, converting

their matter into energy in a way that conserves momentum, energy etc., generating two photons or gamma rays emitted at approximately 180-degree angles [71] which generates a line of response for imaging. PET scanners record coincident gamma rays within a specific detection window (e.g., 4-12 ns) [72]. When opposite detectors within a cylindrical detector ring detect two single photons within the detection window which are opposite to each other, the scanner records this as a coincident event. With the collection of coincident events, lines of response are mathematically calculated, and images are formed based on these detections. Louis Sokoloff is accredited for successfully completing the formation of human brain radioactive isotopes by studying the compound 2-Deoxyglucose (DG), [14C]-DG, and finally his group synthesised 2-[^{18}F]Fluoro-2-Deoxy-D-Glucose (FDG) [73] which is one of the most extensively used radiotracers these days. It marks the uptake of glucose in the tissue and is co-related to the metabolism of certain tissue. The development of cerebral PET imaging and radiotracers aids in the diagnosis, management, and therapy of neurologic illnesses such as Parkinson's disease, dementias, and epilepsy [71]. There are various radiotracers used for assessing different organs. The use of radiolabeled β-amyloid peptide in the early and differential diagnosis of Alzheimer's disease has made significant progress. Amyloid particles are deposited long before acute dementia and is linked to disease development, according to studies using the 11C-Pittsburgh compound B (11C-PiB) [74]. As indicated by animal's tests, following a stroke, two types of activated microglia cells appear in the brain: local activated microglia and remote activated microglia. When a stroke occurs, inflammatory changes are seen in both the local and distant regions of the brain that are related to the stroke-affected area [75]. Thiel et al. [76] utilized diffusion tensor imaging, guided PET using 11C-PK11195, (the binding of which with nervous system is considered to be a useful tool in assessing neuronal damage) to image activated microglia after stroke in patients. After determining the temporal dynamics, relationship was evaluated between the activity of local and remote activated microglia and Pyramidal Tract (PT) damage. All the patients that were studied were undergoing acute poststroke phase and were put in three groups namely control group with no lesion in imaging, PT group with infarc-

tion affecting PT, and non-PT with infarction outside of PT. The results showed that the tracer uptake ratio was initially higher in both the PT and non-PT groups as compared to the control group, but after 6 months, the levels were the same in all the three groups. There were changes in Fractional Anisotropy (FA) that reveal the extent of PT damage following the stroke. [77] The relationship between activated microglia and fibre tract integrity after the stroke was successfully demonstrated for humans in this study. All these radioactive tracers are specifically related to the changes in neural conditions occurring in various diseases. Moving further, the radioactive tracer used currently to measure cerebral perfusion, is [^{15}O]-water which will be discussed in detail in the following paragraphs.

PET using [^{15}O]-gas/water

[^{15}O]-gas/water PET is the gold standard imaging tool for determining cerebral perfusion [78-80]. Although it is a radioactive tracer, the ^{15}O isotope has few features that allow it to be used for non-invasive imaging-based perfusion studies. It has a short half-life, is easily diffusible, and, like ^{129}Xe, is biologically inert. Furthermore, an individual is protected from prolonged radiation dose due to its short half-life. The cerebral metabolic rate of oxygen (CMRO$_2$) and the oxygen extraction fraction are important cerebral physiological indicators for identifying high-risk cerebrovascular sufferers and evaluating brain structure and wellbeing. For [^{15}O]-oxygen PET, two basic delivery techniques have been used: continuous gas inhalation and bolus inhalation [81-84]. The initial experiments used continuous inhalation [81, 82] and after crossing various half-lives of the tracer, PET scans begin, only after an equilibrium was obtained between arterial (supply) and recirculation [1^{5}O]-oxygen and [^{15}O]-water concentrations [85]. In the bolus inhalation approach, [^{15}O]-oxygen is supplied either through a single deep inhale [83] or a short inhalation of up to 1 minute [84].

Not only is ^{129}Xe MRI researched in connection with other types of imaging methods to verify and compare the results, but PET is also studied in conjunction with various MRI techniques. Table 2 summarises all studies in this paper that employed simultaneous PET/^{1}H MRI (comparison tool) measurements and compared ^{1}H MRI with ^{129}Xe brain perfusion MRI techniques.

Table 2: Summary of studies using PET and ^{1}H & ^{129}Xe MRI.

Subject	Diseased/Healthy	PET	^{1}H MRI	^{129}Xe MRI
Humans	Poststroke [76]	Pyramidal tract damage	DTI	-
	Established stroke [64]	-	^{1}H MRI	Brain imaging
	Healthy [11]	-	^{1}H MRI	Brain imaging
	Healthy [65]	-	^{1}H MRI	Brain imaging (co-relation factor)
Animals	Healthy pigs [80]	CBF	(PC MRI)	-
	Healthy pigs [86]	CMRO$_2$	(PMROx)	-
	Healthy baboons[79]	CBF comparison	-	-
	Healthy rats[59, 87]	-	-	Brain Spectra

DTI: Diffusion Tensor Imaging; ^{1}H MRI: Proton Magnetic Resonance Imaging; CBF: Cerebral Blood Flow; PC MRI: Phase Contrast MRI; CMRO$_2$: Cerebral Metabolic Rate of Oxygen; PMROx: PET/MR Imaging of Oxidative Metabolism.

Positron emission tomography employing [15O]-water can be used to quantify Cerebral Blood Flow (CBF), but an Artery Input Function (AIF) acquired from arterial blood sampling is necessary for assessment of regional CBF, which is an intrusive and time-consuming technique. Additionally, without proper cross calibration of the blood measurement detector and the PET scanner, a usable AIF cannot be produced [88]. Invasive arterial blood sampling could be avoided if whole-brain Oxygen Extraction Fraction (OEF) data from MRI could be employed as a scaling factor for simultaneous [15O]-water PET/MRI research [89]. According to preliminary calculations, global scaling of PET images using MRI-derived flow and whole-brain $CMRO_2$ values is resistant to signal changes caused by recirculating water and cerebral blood volume [90].

Numerous studies have showed the application of [15O]-gas/water PET in studying and assessing brain activities. Subramanyam et al. was one of the first groups to measure $CMRO_2$ using PET employing [15O]-labeled tracers and obtained equilibrium brain scans [81] using healthy human volunteers. In a study by Raichle et al., cerebral blood flow was assessed in six adult baboons and a healthy person to determine the accuracy of the PET/autoradiographic approach. Using [15O]-water as a diffusible tracer and injecting it into the carotid artery, the measured value was compared to the true values of CBF. Experiments were successful after a few corrections, and the findings revealed that the values for CBF (true) and CBF (PET) over a blood flow range of (10-155 ml/min/100 g) were pretty close [79]. A study by Mintun et al. on adult baboons measured cerebral OEF and $CMRO_2$ using [15O]-oxygen, CBF using [15O]-water and [15O]-labeled Carbon monoxide ([15O]-CO) was implemented to calculate cerebral blood volume. Thus, a three-tracer technique was developed as well as validated [84]. The use of three tracers at a time makes the quantitative imaging a long procedure of almost 30-60 mins [91]. A one-step procedure was demonstrated by Ohta et al. on nine healthy volunteers to minimise scan time to 3 minutes. It required only a single brief [15O]-gas inhalation and provided a more reliable estimate of cerebral oxygen consumption than the three-tracer method[83] thus eliminating the error caused in quantifications by recirculating water. Kudomi et al. established a system with technology named Dual-tracer Autoradiography (DARG) in which both tracers [15O]-oxygen and [15O]-water are utilised simultaneously to assess OEF, CBF, and $CMRO_2$ during a single PET scan on a continuous presumption of reducing scan duration [92]. The findings were comparable to the three-step traditional approach. The study was conducted on healthy subjects [93] while the validation phase [92] was conducted on monkeys. In this study, a unique formula based on the basis function method [93] was used to abolish the necessity of extra scan for assessing CBV values. To determine the recirculating water content, Kudomi et al. [92] used hand sampling and centrifuge to extract plasma from whole blood. To replace this time-consuming procedure, a new strategy was devised by the group in which content separation was accomplished through the use of linear and model-based methodologies and simulations [94]. Recently, according to the findings of the group, the arterial input functions for the dual-tracer technique can be computed directly from tissue time–activity curves acquired using faster dual tracer PET imaging. The values of CBF, OEF, and $CMRO_2$ obtained through Image-Derived Input Function (IDIF) were consistent with those obtained with the measured arterial input function [95]. This finding implies that non-invasive assessment of CBF, OEF, and $CMRO_2$ is possible. Figure 5 represents the maps obtained by both methods.
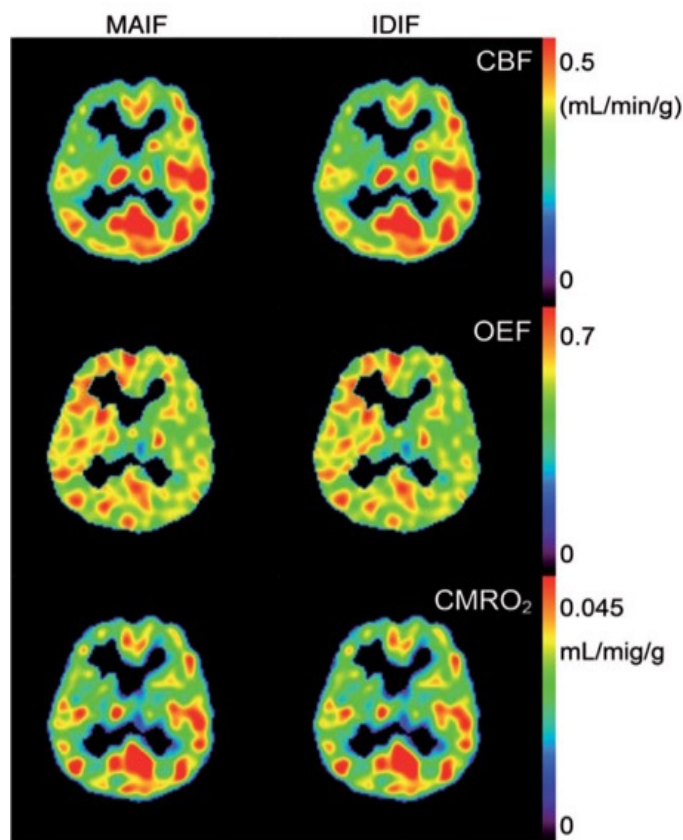

Figure 5: The values of CBF, OEF and $CMRO_2$ are showing similar values as obtained by both measured arterial input function and estimated Image-derived input function (IDIF) techniques. Figure was adapted from [95].

Furthermore, in a study by Kuttner et al. [88], AIF measurements for CBF PET in human subjects consisting of both patients with multiple sclerosis and healthy volunteers, were compared using a non-invasive technique for input function prediction based on machine learning. According to the findings, both approaches produced similar conclusions, and the associated CBF values were closely correlated and effectively distinguishable before and after medication. In a recent study, Ssali et al. [80] developed a hybrid and non-invasive approach for measuring CBF utilising phase contrast magnetic resonance imaging (PC-MRI) and [15O]-water PET at the same time, eliminating noise and arterial sampling. The study was conducted on healthy pigs with CBF measurements recorded under two of the three possible $PaCO_2$ levels (hyper-, normo-, and hypercapnia). Normocapnia is a state depicting normal arterial carbon dioxide pressure. Hypercapnia is a buildup of carbon dioxide in the blood while Hypocapnia depicts the the lowering of CO_2 in the bloodstream. Figure 6 shows the comparison of images obtained by PET alone as well as referenced MR image corresponding to each level.

With a correlation value of 0.9 and a slope of 0.88, the results for CBF from both [15O]-water PET and PC-MRI were strongly correlated [80]. This non-invasive PET/MRI hybrid strategy would be advantageous for those for whom establishing correct CBF using existing modalities is difficult. In order to minimize invasiveness and measurement duration of $CMRO_2$ [91], a study by Narciso et al. [86], proposed a new technique named PET/MR imaging of oxidative metabolism (PMROx) which does not need arterial sampling avoiding many of the complications of PET $CMRO_2$. An MRI technique was used to measure whole-brain $CMRO_2$ which further acted as a reference to calibrate [15O]-oxygen data.

These studies [80,86,91] indicated that [^{15}O]-water PET/ ^{1}H MRI has been successfully used to quantify cerebral blood flow and evaluate oxygen extraction fraction and cerebral metabolic rate of oxygen, in porcine brains, and this work is being translated to humans.

Typical parameters used in ^{129}xe MRI and PET

Table 3 highlights the typical parameters utilised in $^{15}O_2$ PET and ^{129}Xe/^{1}H MRI measurements in the studies discussed in this article.
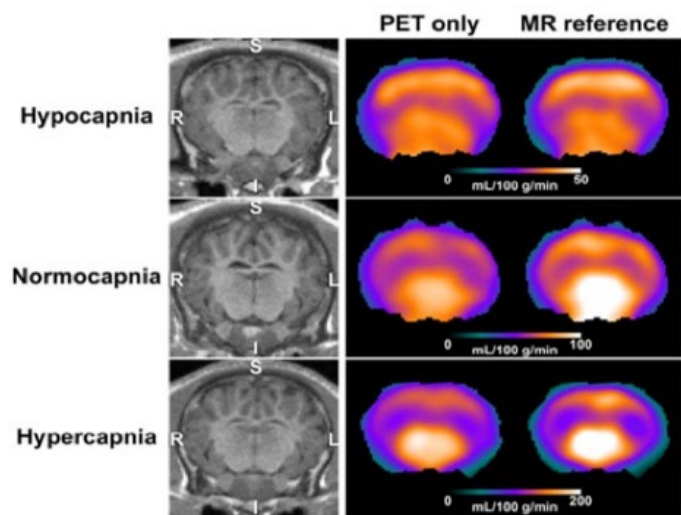

Figure 6: The assessment of cerebral blood flow in animals at three different P_aCO_2 levels, namely Hypocapnia, Normocapnia, and Hypercapnia, is illustrated using PET, with separate reference pictures produced using the MRI approach. T_1-weighted pictures on the left can be used to reference both of these methods anatomically. The letters I and S stand for inferior and superior, respectively. Figure was adapted from [80].

Table 3: Typical Acquisition Parameters for ^{129}Xe MRI, ^{1}H MRI and PET.

Parameters	^{129}Xe MRI	^{1}H MRI
TE/TR	1.7 msec/34 msec	15 msec/4 sec
FOV	22 cm	24 cm
Matrix size	32 x 32	80 x 80
FA	12.5^0	40^0
BW	4 kHz	16 kHz
Frequency	17.6 MHz	63.5 MHz
Pulse Sequence	2D Spoiled GE	EPI
Parameters	**PET values for brain imaging**	
Reconstruction Method	Iterative	
Iterations	6	
Filter	Gaussian	
Zoom factor	2	
Subsets	16	
Image size(pixels)	256	

TE/TR: Echo time/Repetition time; FOV: Field of View; FA: Flip Angle; BW: Band Width; GE: Gradient Echo; EPI: Echo Planar imaging.

Most of the studies used in this paper, conducted by Rao et al. [11,64,65] basically used two dimensional spoiled gradient-echo pulse sequence at 1.5 T with the following parameters for brain imaging; xenon-129 frequency = 1.76 MHz (198 ppm downfield from the ^{129}Xe gas resonance); Echo Time (TE) = 1.7 ms; repetition time (TR) = 34 ms; flip angle (FA) = 12.5; Bandwidth (BW) = 4 kHz; field of view (FOV) = 22 x 22 cm^2. While at the same time the parameters used for the comparison technique; ^{1}H MRI are Gradient echo EPI; Field Of View (FOV) = 24 x 24 cm^2; slice thickness =7 mm, flip angle = 40°, TE = 14 ms, TR = 4.25 s and labeling duration of 1650 msec.

On the other hand, for carrying out PET scans of brain, iterative method of reconstruction is used with Gaussian filter. 16 subsets are basically required with an image size of 256 pixels. OSEM: Ordered Subset Expectation Maximization, is a type of iterative reconstruction used to reconstruct 3D PET data from the coincident counts detected by the PET system. The most important parameter in PET is the acquisition time.

PET & ^{129}xe MRI: Challenges, Limitations and Opportunities

Table 4 presents an overview of the obstacles, constraints, and potential related with PET and ^{129}Xe MRI.

Table 4: Challenges, limitations and opportunities.

	PET	^{129}Xe-MRI
Challenges	High Operating Cost; Low Resolution; Slow in data acquisition Requires CYCLOTRON, radiation safety control	Low SNR; Requires xenon polarizer, Broadband xenon RF amplifier, RF coil tuned on the ^{129}Xe frequency
Limitations	Use radioactive tracer; not suitable for pregnant women and kids; Short half-life of O$^{15;}$ Unable to pick up rapid changes in brain activity	Low spatial resolution; Low solubility in tissues; Short T1 in blood; Affected by physiological state of lungs; Not-validated for the perfusion imaging in brain
Opportunities	Clinical Gold Standard; High molecular sensitivity; High temporal resolution; Can be used in combination with CT and MRI images; Faster diagnosis of diseases	FDA Approved (gas phase pulmonary measurements); Non-invasive; Free of ionizing radiation; High polarization; Naturally abundant, Comparatively low cost

SNR: Signal-to-noise ratio; FDA: Food and Drug Administration.

PET has a higher cost and takes longer to acquire images, but it has a better quality and is preferable for early medical diagnostics. ^{129}Xe MRI, on the other hand, despite the limited Signal-to-Noise Ratio (SNR) and spatial clarity, is a non-invasive methodology with a low price resulting from environmental richness of ^{129}Xe. At the molecular level, PET/MRI is a powerful imaging technique that can give complementary functional and structural details regarding any particular organ or bodily system [96]. Although PET is the gold standard [91] diagnostic tool for assessing cerebral perfusion [79,80] in clinical settings but because of its utilization of radio tracers, it is harmful to be used for diagnosis of pregnant women and children. ^{129}Xe MRI, on the other hand, is a patient-friendly, radiation-free imaging approach that will be approved by the FDA soon for gas phase pulmonary measures but has yet to be established for brain perfusion imaging. Even though these techniques are well-established, they each have significant limitations, PET relies on the injection of radioactive contrast agents, and the resulting PET images are limited in resolution [97] while ^{129}Xe based MR

images have low SNR. Though complex technology is required, the cost of [129]Xe MRI is far lower than that of PET due to its natural abundance [1]. By enhancing sensitivity over other MRI methods and extending beyond the resolution constraints of PET, [129]Xe-based imaging could alter the ways of mapping grey and white matter [59,62,87], perfusion [11], and targeted drug and cell tracking techniques [98]. Because of its verification with gold standard [15O]-water PET, our new pre-clinical investigation has the potential to overcome the barrier and enable quantitative [129]Xe based clinical imaging approaches in the future.

Future directions

[129]Xe-based brain perfusions have been measured using [1]H Arterial spin labelling, but the technology has yet to be validated against gold standard imaging techniques like Positron Emission Tomography (PET). Although both gases, [129]Xe and oxygen, are dissolved along the barrier tissues and bind to red blood cells as they travel through the lungs to the brain, [129]Xe's unique solubility and chemical shift for the gas and dissolved phases makes it a preferable alternative and promising contrast agent. Figure 7 represents the successful demonstration of the simultaneous measurements of hyperpolarized [129]Xe MRI and [15O]-water PET done by our group.
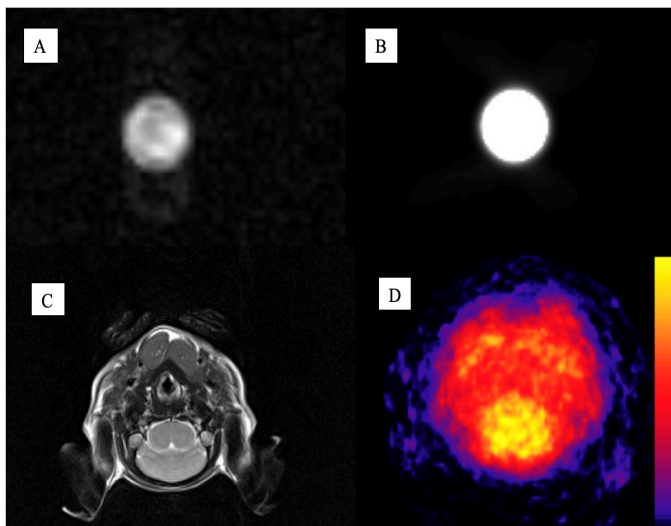

Figure 7: Panels A, B, and C, D represents as follows: 2D axial A) [129]Xe MRI image, B) [15O]-water PET image obtained for xenon dissolved in [15O]-water inside the syringe phantom, C) ^{1}H image and D) [15O]-water PET perfusion image obtained from rat brain.

To our knowledge, this is the first time a global successful demonstration of [129]Xe when dissolved in [15O]-water can be employed in multi-modal imaging [99]. Phantom PET/[129]Xe MRI measurements were taken during the validation phase. 30mL of hyperpolarized [129]Xe gas was dissolved in 30mL of [15O]-water while shaking for 10 seconds in a 60 mL plastic syringe. For in-vivo measurements, rats were induced with 5% isoflurane and oxygen and maintained at 2%. A 24 g tail vein catheter was inserted for delivery of the [15O]- water / [129]Xe mixture. Once prepared, rats were transferred to a custom animal bed that interfaces with the PET insert animal positioning system and couples with the inserted RF coils, co-localizing the rat brain for all modalities. Hyperpolarized [129]Xe gas was obtained from a turn-key, spin-exchange polarizer system (Polarean 9800 [129]Xe polarizer). The initial [129]Xe polarization was 15%. [129]Xe dissolved phase images were acquired in a 3T PET/MRI (Siemens Biograph mMR, Siemens Healthineers, Erlangen, Germany) scanner using whole-body gradients and a homebuilt rat-sized RF coil tuned

to 34.09 MHz. A Fast-Gradient-Recalled-Echo sequence was utilized for phantom (Matrix Size=64x64; Slice thickness=250 mm; TE/TR=2.04/20 ms; BW=660 Hz/pixel; Flip angle=11° FOV=150 x 150 mm^2) and rat (Matrix Size=64 x 64; Slice thickness=250 mm; TE/TR=3.44/100ms; BW=660 Hz/pixel; Flip angle=11° FOV=70 x 70 mm^2) scans Three consecutive axial images were acquired during the PET scan. The total scan time was 1sec per image for the phantom and 14sec for rat. [15O]-water PET data (half-life-time of 2 min) were acquired simultaneously with [129]Xe MRI for 600 sec using the integrated PET system in the 3T PET/MRI. PET data were reconstructed into ten 60 sec frames using a 3D iterative routine (OSEM) with three iterations, 21 subsets, in-plane resolution of 1.04 x 1.04 mm^2 and a slice thickness of 2.03 mm. PET imaging was obtained using a small animal MRI compatible PET insert (Cubresa Inc.) (Figure 1) with an FOV of 58.9 mm (trans-axial) by 67.2 mm (axial). We waited until the 0.5 mL xenon/water mixture was 25 MBq, then injected into the tail vein. PET data were reconstructed into ten 120 sec frames using a 3D iterative routine (OSMAPOSL) with eight iterations, 25 subsets, in-plane resolution of 1.04 x 1.04 mm^2 and a slice thickness of 2.03mm. Figure 7 shows A) 2D axial [129]Xe MRI images and B) [15O]-water PET images acquired simultaneously. [129]Xe/PET images indicate that the diameter of the phantom from both PET and MRI images are similar. The [129]Xe image demonstrates a sufficient SNR level (80) suggesting that 3D [129]Xe imaging is possible. Figure 7C and 7D shows the anatomical-proton and [15O]-water PET perfusion images of rat-brain [100]. The in-vivo demonstration did not bring the desired [129]Xe image quality because of various reasons. In general, it is a very complicated measurement which is hard to execute considering a synchronization of the two tracers preparation mixing and injection. There was a time delay between the usage of both tracers leading to the significant polarization decay of the [129]Xe gas from the initial 15% polarization to 7% at the time of mixing and injecting. We plan to significantly increase the initial xenon polarization (up to 50%) and minimize the xenon-waiting-time.

It is well known that [129]Xe lung MRI is currently used as a clinical tool in the United Kingdom [101]. The North-American xenon consortium [102] got FDA (Food and Drug Administration) approval recently, and this will now allow better diagnoses, clinical judgement, and treatment assessment of patients suffering from severe lung, cardiac, and neurological illnesses in Canada and worldwide. Since the potential of side by side measurements of both hyperpolarized [129]Xe MRI and [15O]-water PET has been effectively verified, we propose to probe a rat model with subcortical stroke to identify the role of ageing and disease on white matter and neuroplasticity at the microstructural levels, during the full scope of its evaluation from infancy to late adulthood.

These days high-quality data acquisitions, administering lower doses has been made possible with latest polarization technologies [6], specialised RF coil designs, and MR pulse sequence optimization [103] Continuous flow polarizer is the best choice for MR applications of hyperpolarized [129]Xe in a clinical setting, as it is necessary to get a large production rate of around 1litre/hr in order to produce high quantities of [129]Xe. While 2D spoiled gradient echo (SPGR) can be utilised for imaging, radial [104] and spiral [105,106] k-space acquisition enables [129]Xe gas imaging with high temporal resolution. Multi-tuned RF coils [107,108] or switchable-resonance RF coils [109,110] can be utilised to establish spatially concordance of ^{1}H and [129]Xe images, which is important for clinical assessment.

Deep Learning (DL) employing convolutional neural networks has recently exhibited unprecedented performance in a variety of medical imaging applications, including image separation and classification [111]. In a recent study [112], deep convolutional neural network was used to simulate CT and MRI scans. Also, the similar approach was used to produce lung ventilation maps that highly correlated with noble gas MRI and pulmonary function data [111]. We believe that using an analogous strategy, deep learning may be able to convert [129]Xe perfusion images into PET images.

In addition, we believe that the development and approval of [129]Xe MRI will enable the use of a relatively cheap and non-radioactive tracer for clinical lung & brain perfusion measurements. Since many cancer, stroke, and COVID-19 patients require blood perfusion scans for treatment assessment/planning, this would have significant economic benefits taking into account that [129]Xe MRI is the imaging modality permitting high resolution lung structure & function and brain perfusion measurements without the need for a radioactive tracer, and therefore, the need for a very expensive cyclotron facility. In doing so, it may enhance the accessibility of such diagnostic and treatment assessment/planning.

To conclude, we have successfully demonstrated the acquisition of hyperpolarized [129]Xe MRI and [^{15}O]-water PET data at the same time. PET-MRI hybrid advancements will improve our understanding of cerebral processes and may aid in monitoring clinical outcomes and treatments. The potential of employing [129]Xe as a non-radioactive tracer and high-resolution imaging tool that provides similar and complementary information to [^{15}O]-PET might be a far more cost-effective substitute to PET for imaging stroke, brain cancer, and other brain diseases such as Alzheimer disease, vascular dementia, and brain ischemia, and will considerably raise the capacity of [129]Xe MRI medical applications.

References

1. Miller KW, et al. Xenon NMR: Cemical shifts of a general anesthetic in common solvents, proteins, and membranes. Proceedings of the National Academy of Sciences. 1981; 78: 4946-4949.

2. Raftery D. Xenon NMR Spectroscopy, in Annual Reports on NMR Spectroscopy, G.A. Webb, Editor. 2006, Academic Press. 205-270.

3. Moller, H.E, et al. MRI of the lungs using hyperpolarized noble gases. Magn Reson Med. 2002; 47: 1029-51.

4. Chen XJ, et al. Spatially resolved measurements of hyperpolarized gas properties in the lung in vivo. Part I: Diffusion coefficient. Magnetic Resonance in Medicine. 1999; 42: 721-728.

5. Hersman FW, et al. Large production system for hyperpolarized 129Xe for human lung imaging studies. Acad Radiol. 2008; 15: 683-92.

6. Marshall H, et al. In vivo methods and applications of xenon-129 magnetic resonance. Progress in Nuclear Magnetic Resonance Spectroscopy. 2021; 122: 42-62.

7. Goto T, et al. Minimum alveolar concentration-awake of Xenon alone and in combination with isoflurane or sevoflurane. Anesthesiology. 2000; 93: 1188-93.

8. LUTTROPP, H.H, et al. Clinical experience with minimal flow xenon anesthesia. Acta Anaesthesiologica Scandinavica. 1994; 38: 121-125.

9. Fox MS, MJ Couch, MS Albert. Chapter 22 Magnetic Resonance Imaging of the Brain using Hyperpolarized 129Xe, in Hyperpolarized Xenon-129 Magnetic Resonance: Concepts, Production, Techniques and Applications. 2015, The Royal Society of Chemistry. 2015; 407-425.

10. Shukla Y, et al. Hyperpolarized 129Xe magnetic resonance imaging: tolerability in healthy volunteers and subjects with pulmonary disease. Acad Radiol. 2012. 19: 941-51.

11. Rao MR, et al. Imaging Human Brain Perfusion with Inhaled Hyperpolarized (129)Xe MR Imaging. Radiology. 2018; 286: 659-665.

12. Fox M, A Ouriadov. High Resolution 3He Pulmonary MRI, in Magnetic Resonance Imaging, A.P.L. Manchev, Editor. 2019, IntechOpen Limited: London, UK. 2019.

13. Mugler JP. 3rd and T.A. Altes, Hyperpolarized 129Xe MRI of the human lung. J Magn Reson Imaging. 2013. 37: 313-31.

14. Happer W, et al. Polarization of the nuclear spins of noble-gas atoms by spin exchange with optically pumped alkali-metal atoms. Physical Review A. 1984; 29: 3092-3110.

15. Bouchiat MA, TR Carver, CM Varnum. Nuclear Polarization inHe-3Gas Induced by Optical Pumping and Dipolar Exchange. Physical Review Letters. 1960; 5: 373-375.

16. Kauczor HU, R Surkau, T Roberts. MRI using hyperpolarized noble gases. European Radiology. 1998; 8: 820-827.

17. Roos JE, et al. Hyperpolarized Gas MR Imaging: Technique and Applications. Magnetic resonance imaging clinics of North America. 2015; 23: p. 217-229.

18. Polarean 9820 129Xe Hyperpolarizer. Polarean Inc. 2016.

19. Nikolaou P, et al. A 3D-Printed High Power Nuclear Spin Polarizer. Journal of the American Chemical Society, 2014. 136: 1636-1642.

20. Schrank G, et al. Characterization of a low-pressure high-capacity $^{129}\text{X}\text{e}$ flow-through polarizer. Physical Review A, 2009. 80: 063424.

21. Korchak SE, W Kilian, L Mitschang. Configuration and Performance of a Mobile (129)Xe Polarizer. Appl Magn Reson. 2013; 44: 65-80.

22. Patz S, et al. Hyperpolarized (129)Xe MRI: a viable functional lung imaging modality? Eur J Radiol, 2007. 64(3): p. 335-44.

23. Norquay, G, et al. Large-scale production of highly-polarized 129Xe [abstract]. Proceedings of the 25th Annual Meeting of ISMRM, Hawaii, USA. 2017: p. 2140.

24. Norquay G, NJ Stewart, JM Wild. Approaching the theoretical limit for 129Xe hyperpolarisation with continuous-flow spin-exchange optical pumping [abstract] Proceedings of the 23th Annual Meeting of ISMRM, Toronto, Canada. 2015: 1505.

25. Kaushik SS, et al. Single-breath clinical imaging of hyperpolarized (129)Xe in the airspaces, barrier, and red blood cells using an interleaved 3D radial 1-point Dixon acquisition. Magn Reson Med. 2016; 75: 1434-43.

26. Bartel SE, et al. Role of collateral paths in long-range diffusion in lungs. J Appl Physiol (1985), 2008; 104: 1495-503.

27. Nikolaou P, et al. A 3D-printed high power nuclear spin polarizer. J Am Chem Soc. 2014; 136: 1636-42.

28. Albert MS, et al. Biological magnetic resonance imaging using laser-polarized 129Xe. Nature. 1994; 370: 199-201.

29. Virgincar RS, et al. Quantitative analysis of hyperpolarized 129Xe ventilation imaging in healthy volunteers and subjects with chronic obstructive pulmonary disease. NMR in biomedicine. 2013; 26: 424-435.

30. He, M, et al. Extending semiautomatic ventilation defect analysis for hyperpolarized (129Xe) ventilation MRI. Academic radiology. 2014; 21: 1530-1541.

31. Ebner L, et al. Hyperpolarized 129Xenon Magnetic Resonance Imaging to Quantify Regional Ventilation Differences in Mild to Moderate Asthma: A Prospective Comparison Between Semiautomated Ventilation Defect Percentage Calculation and Pulmonary Function Tests. Investigative radiology, 2017. 52:120-127.

32. Thomen RP, et al. Hyperpolarized (129)Xe for investigation of mild cystic fibrosis lung disease in pediatric patients. J Cyst Fibros, 2017. 16: 275-282.

33. Mathew, L, et al. Hyperpolarized 3He magnetic resonance imaging: Preliminary evaluation of phenotyping potential in chronic obstructive pulmonary disease. European Journal of Radiology. 2011; 79: 140-146.

34. He M, et al. Using Hyperpolarized 129Xe MRI to Quantify the Pulmonary Ventilation Distribution. Academic Radiology. 2016; 23: 1521-1531.

35. Kirby M, et al. Hyperpolarized 3He and 129Xe MR Imaging in Healthy Volunteers and Patients with Chronic Obstructive Pulmonary Disease. Radiology. 2012; 265: 600-610.

36. Ebner L, et al. Multireader Determination of Clinically Significant Obstruction Using Hyperpolarized 129Xe-Ventilation MRI. American Journal of Roentgenology. 2019; 212: 758-765.

37. Stewart NJ, et al. Comparison of 3He and 129Xe MRI for evaluation of lung microstructure and ventilation at 1.5T. Journal of Magnetic Resonance Imaging. 2018; 48: p. 632-642.

38. Qing K, K Ruppert. Chapter 11 - Hyperpolarized Xenon-129 Dissolved-Phase Magnetic Resonance Imaging A2 - Albert, Mitchell S, in Hyperpolarized and Inert Gas MRI, F.T. Hane, Editor. 2017, Academic Press: Boston. 2017; 169-181.

39. Fox MS, et al. Detection of radiation induced lung injury in rats using dynamic hyperpolarized (129)Xe magnetic resonance spectroscopy. Med Phys. 2014; 41: 072302.

40. Zanette B, et al. Detection of regional radiation-induced lung injury using hyperpolarized (129)Xe chemical shift imaging in a rat model involving partial lung irradiation: Proof-of-concept demonstration. Advances in radiation oncology. 2017; 2: 475-484.

41. Driehuys B, et al. Pulmonary perfusion and xenon gas exchange in rats: MR imaging with intravenous injection of hyperpolarized 129Xe. Radiology. 2009; 252: p. 386-93.

42. Ruppert K, et al. Using Hyperpolarized Xenon-129 MRI to Quantify Early-Stage Lung Disease in Smokers. Academic radiology. 2019; 26: 355-366.

43. Qing K, et al. Assessment of lung function in asthma and COPD using hyperpolarized 129Xe chemical shift saturation recovery spectroscopy and dissolved-phase MRI. NMR Biomed. 2014; 27: 1490-501.

44. Driehuys B, et al. Imaging alveolar-capillary gas transfer using hyperpolarized 129Xe MRI. Proceedings of the National Academy of Sciences. 2006; 103: 18278-18283.

45. Mugler, J.P, 3rd, et al. Simultaneous magnetic resonance imaging of ventilation distribution and gas uptake in the human lung using hyperpolarized xenon-129. Proc Natl Acad Sci U S A. 2010; 107: 21707-12.

46. Iguchi, S, et al. Direct imaging of hyperpolarized 129Xe alveolar gas uptake in a mouse model of emphysema. Magn Reson Med. 2013; 70: 207-15.

47. Swanson SD, et al. Distribution and dynamics of laser-polarized (129)Xe magnetization in vivo. Magn Reson Med. 1999; 42: 1137-45.

48. Cleveland ZI, et al. Hyperpolarized Xe MR imaging of alveolar gas uptake in humans. PLoS One. 2010. 5: e12192.

49. Chacon-Caldera, J, et al. Dissolved hyperpolarized xenon-129 MRI in human kidneys. Magn Reson Med. 2020. 83: 262-270.

50. Zöllner FG, et al. Functional imaging of acute kidney injury at 3 Tesla: Investigating multiple parameters using DCE-MRI and a two-compartment filtration model. Z Med Phys. 2015; 25: 58-65.

51. Zimmer, F, et al. Quantitative arterial spin labelling perfusion measurements in rat models of renal transplantation and acute kidney injury at 3T. Z Med Phys. 2017; 27: 39-48.

52. Gutjahr, F.T, et al. MRI-based quantification of renal perfusion in mice: Improving sensitivity and stability in FAIR ASL. Z Med Phys. 2017; 27: 334-339.

53. Zhang JL, et al. Functional MRI of the kidneys. J Magn Reson Imaging. 2013; 37: 282-93.

54. Martirosian, P, et al. FAIR true-FISP perfusion imaging of the kidneys. Magn Reson Med. 2004; 51: 353-61.

55. Norquay G, et al. Relaxation and exchange dynamics of hyperpolarized 129Xe in human blood. Magn Reson Med. 2015; 74: 303-11.

56. Mugler J, et al. Imaging of dissolved-phase hyperpolarized xenon-129 in human kidneys. Int Soc Magn Reson Med, Toronto, Canada. 2015.

57. Miller G, et al. Dynamic spectroscopy of dissolved-phase xenon-129 in the human kidney. in Proc Intl Soc Mag Reson Med. 2017.

58. Swanson SD, et al. Brain MRI with laser-polarized 129Xe. Magn Reson Med. 1997; 38: 695-8.

59. Wakai A, et al. In vivo MR spectroscopy of hyperpolarized Xe-129 in rat brain. International Congress Series. 2004; 1265: 139-143.

60. Welsh RC, et al. Magnetic resonance imaging with laser-polarized 129Xe. Nuclear Instruments and Methods in Physics Research Section A: Accelerators, Spectrometers, Detectors and Associated Equipment. 1998; 402: 461-463.

61. Kershaw J, et al. Confirming the existence of five peaks in 129Xe rat head spectra. Magn Reson Med. 2007; 57: 791-7.

62. Mugler JP, 3rd, et al. MR imaging and spectroscopy using hyperpolarized 129Xe gas: Preliminary human results. Magn Reson Med. 1997; 37: 809-15.

63. Abbott NJ, L Ronnback, E Hansson. Astrocyte-endothelial interactions at the blood-brain barrier. Nat Rev Neurosci, 2006. 7(1): p. 41-53.

64. Rao MR, et al. Assessment of brain perfusion using hyperpolarized 129Xe MRI in a subject with established stroke. Journal of Magnetic Resonance Imaging. 2019; 50: 1002-1004.

65. Rao M, G Norquay, JM Wild. Investigating gas-exchange and tissue perfusion in the human brain using a combination of proton

and hyperpolarized xenon-129 MRI. Proceedings of the 27th Annual Meeting of ISMRM, Montreal, Canada. 2019: 3095.

66. Zhou X, et al. MRI of stroke using hyperpolarized 129Xe. NMR in Biomedicine. 2011. 24: 170-175.

67. Mazzanti ML, et al. Distribution of Hyperpolarized Xenon in the Brain Following Sensory Stimulation: Preliminary MRI Findings. PLOS ONE. 2011; 6: e21607.

68. Shepelytskyi, Y, et al. Hyperpolarized (129) Xe imaging of the brain: Achievements and future challenges. Magn Reson Med, 2022. 88: p. 83-105.

69. Rao, M.R, et al. Measuring (129) Xe transfer across the blood-brain barrier using MR spectroscopy. Magn Reson Med, 2021. 85: p. 2939-2949.

70. Friedlander, Y, et al. Hyperpolarized 129Xe MRI of the rat brain with chemical shift saturation recovery and spiral-IDEAL readout. Magnetic Resonance in Medicine, 2022. 87: 1971-1979.

71. Portnow LH, DE Vaillancourt, MS Okun. The history of cerebral PET scanning: from physiology to cutting-edge technology. Neurology. 2013 80: 952-956.

72. Shukla AK, U Kumar. Positron emission tomography: An overview. Journal of medical physics. 2006; 31: 13-21.

73. Dienel GA. In memoriam Louis Sokoloff, M.D. 1921-2015. Journal of cerebral blood flow and metabolism: Official journal of the International Society of Cerebral Blood Flow and Metabolism. 2016; 36: 278-280.

74. Ferreira LK, GF Busatto. Neuroimaging in Alzheimer's disease: current role in clinical practice and potential future applications. Clinics (Sao Paulo). 2011; 19-24.

75. Myers R, et al. [3H] PK 11195 and the localisation of secondary thalamic lesions following focal ischaemia in rat motor cortex. Neurosci Lett. 1991; 133: 20-4.

76. Thiel A, et al. The temporal dynamics of poststroke neuroinflammation: A longitudinal diffusion tensor imaging-guided PET study with 11C-PK11195 in acute subcortical stroke. J Nucl Med. 2010; 51: 1404-12.

77. Liang Z, et al. A prospective study of secondary degeneration following subcortical infarction using diffusion tensor imaging. J Neurol Neurosurg Psychiatry. 2007; 78: 581-6.

78. Fan AP, et al. Comparison of cerebral blood flow measurement with [15O]-water positron emission tomography and arterial spin labeling magnetic resonance imaging: A systematic review. J Cereb Blood Flow Metab. 2016; 36: 842-61.

79. Raichle ME, et al. Brain blood flow measured with intravenous H2(15) O. II. Implementation and validation. J Nucl Med. 1983; 24: 790-8.

80. Ssali T, et al. A Noninvasive Method for Quantifying Cerebral Blood Flow by Hybrid PET/MRI. J Nucl Med. 2018; 59: 1329-1334.

81. Subramanyam R, et al. A MODEL FOR REGIONAL CEREBRAL OXYGEN DISTRIBUTION DURING CONTINUOUS INHALATION OF 15O2, C15O. AND C15O2. Journal of Computer Assisted Tomography. 1978; 2: 671.

82. Frackowiak RSJ, et al. Quantitative Measurement of Regional Cerebral Blood Flow and Oxygen Metabolism in Man Using 15O and Positron Emission Tomography: Theory, Procedure, and Normal Values. Journal of Computer Assisted Tomography. 1980; 4: 727-736.

83. Ohta S, et al. Oxygen consumption of the living human brain measured after a single inhalation of positron emitting oxygen. J Cereb Blood Flow Metab. 1992; 12: 179-92.

84. Mintun MA, et al. Brain oxygen utilization measured with O-15 radiotracers and positron emission tomography. J Nucl Med. 1984; 25: 177-87.

85. Fan AP, et al. Quantification of brain oxygen extraction and metabolism with [15O]-gas PET: A technical review in the era of PET/MRI. NeuroImage. 2020. 220: 117136.

86. Narciso L, et al. A Noninvasive Method for Quantifying Cerebral Metabolic Rate of Oxygen by Hybrid PET/MRI: Validation in a Porcine Model. J Nucl Med. 2021.

87. Kershaw J, et al. Confirming the existence of five peaks in 129Xe rat head spectra. Magnetic Resonance in Medicine, 2007. 57: 791-797.

88. Kuttner S, et al. Cerebral blood flow measurements with (15) O-water PET using a non-invasive machine-learning-derived arterial input function. J Cereb Blood Flow Metab. 2021; 271678x21991393.

89. Ishii Y, et al. Simultaneous phase-contrast MRI and PET for non-invasive quantification of cerebral blood flow and reactivity in healthy subjects and patients with cerebrovascular disease. Journal of Magnetic Resonance Imaging. 2020; 51: 183-194.

90. Narciso L, et al. Initial assessment of a reference-based non-invasive hybrid PET/MRI method for imaging CMRO2. J. Cerebr. Blood Flow Metabol. 2019; 39: 572-573.

91. Narciso L, et al. A non-invasive reference-based method for imaging the cerebral metabolic rate of oxygen by PET/MR: theory and error analysis. Phys Med Biol, 2021. 66: 065009.

92. Kudomi N, et al. Rapid quantitative measurement of CMRO (2) and CBF by dual administration of (15) O-labeled oxygen and water during a single PET scan-a validation study and error analysis in anesthetized monkeys. J Cereb Blood Flow Metab. 2005; 25: 1209-24.

93. Kudomi N, et al. Rapid quantitative CBF and CMRO (2) measurements from a single PET scan with sequential administration of dual (15)O-labeled tracers. J Cereb Blood Flow Metab. 2013. 33: 440-8.

94. Kudomi N, et al. Separation of input function for rapid measurement of quantitative CMRO2 and CBF in a single PET scan with a dual tracer administration method. Phys Med Biol. 2007; 52: 1893-908.

95. Kudomi N, et al. Reconstruction of input functions from a dynamic PET image with sequential administration of (15) O2 and [Formula: See text] for noninvasive and ultra-rapid measurement of CBF, OEF, and CMRO2. J Cereb Blood Flow Metab. 2018; 38: 780-792.

96. Jung, J.H, Y. Choi, and K.C. Im, PET/MRI: Technical Challenges and Recent Advances. Nuclear medicine and molecular imaging. 2016; 50: 3-12.

97. Shepelytskyi Y, et al. Hyperpolarized (129)Xe Time-of-Flight MR Imaging of Perfusion and Brain Function. Diagnostics (Basel, Switzerland). 2020; 10: 630.

98. Zhang B, et al. An intracellular diamine oxidase triggered hyperpolarized (129)Xe magnetic resonance biosensor. Chem Commun (Camb). 2018. 54: 13654-13657.

99. Sembhi R, et al. Study proving Feasibility of Simultaneous Hyperpolarized 129Xe MRI and [15O]-water PET Measurements. World Molecular Imaging Society, Miami, Florida, USA (2021).

2021.

100. Sembhi R, et al. In-Vivo Simultaneous Hyperpolarized 129Xe MRI and [15O]-water PET Multi-Modal Imaging: A Proof of Concept Study. Proceedings of the 32nd Annual Meeting of ISMRM, Toronto, Canada. 2023.

101. Wild J, et al. P283 Hyperpolarised Gas MRI-a pathway to Clinical Diagnostic Imaging. Thorax. 2015; 70: A220-A221.

102. Ouriadov A, et al. Lung morphometry using hyperpolarized (129) Xe apparent diffusion coefficient anisotropy in chronic obstructive pulmonary disease. Magn Reson Med. 2013; 70: 1699-706.

103. Stewart NJ, et al. Feasibility of human lung ventilation imaging using highly polarized naturally abundant xenon and optimized three-dimensional steady-state free precession. Magnetic Resonance in Medicine. 2015. 74: 346-352.

104. Wild JM, et al. Dynamic radial projection MRI of inhaled hyperpolarized 3He gas. Magn Reson Med. 2003. 49: 991-7.

105. Salerno M, et al, Dynamic spiral MRI of pulmonary gas flow using hyperpolarized (3)He: Preliminary studies in healthy and diseased lungs. Magn Reson Med. 2001. 46: 667-77.

106. Doganay O, et al, Fast dynamic ventilation MRI of hyperpolarized (129) Xe using spiral imaging. Magn Reson Med. 2018; 79: 2597-2606.

107. Shen GX, FE Boada, KR Thulborn. Dual-frequency, dual-quadrature, birdcage RF coil design with identical b1 pattern for sodium and proton imaging of the human brain at 1.5 T. Magnetic Resonance in Medicine, 1997; 38: 717-725.

108. Matson GB, P Vermathen, TC Hill. A practical double-tuned 1H/31P quadrature birdcage headcoil optimized for 31P operation. Magn Reson Med. 1999; 42: 173-82.

109. Maunder A, et al. Comparison of MEMS switches and PIN diodes for switched dual tuned RF coils. Magnetic Resonance in Medicine. 2018; 80: 1746-1753.

110. Ha S, et al. A PIN diode controlled dual-tuned MRI RF coil and phased array for multi nuclear imaging. Phys Med Biol. 2010. 55: 2589-600.

111. Capaldi DPI, et al. Pulmonary Ventilation Maps Generated with Free-breathing Proton MRI and a Deep Convolutional Neural Network. Radiology. 2021; 298: 427-438.

112. Han X. MR-based synthetic CT generation using a deep convolutional neural network method. Med Phy. 2017; 44: 1408-1419.